Computational Materials Science 68 (2013) 245–254

Contents lists available at SciVerse ScienceDirect

Computational Materials Science

journal homepage: www.elsevier.com/locate/commatsci

Hypervelocity impact of copper nano-projectiles on copper

N. Amigo [a,*], C. Loyola [a,b], S. Davis [a], G. Gutiérrez [a]

[a] Grupo de NanoMateriales, Departamento de Física, Facultad de Ciencias, Universidad de Chile, Casilla 653, Santiago, Chile
[b] Department of Materials Science and Engineering, Iowa State University, USA

ARTICLE INFO

Article history:
Received 10 July 2012
Received in revised form 4 November 2012
Accepted 5 November 2012
Available online 4 December 2012

Keywords:
Molecular dynamics
Hypervelocity impact
Non-equilibrium

ABSTRACT

An atomic-level simulation of the collisions between a nano-projectile against a target, both composed of copper, is presented. The study is performed by means of molecular dynamics simulations, in a system at a temperature of 300 K, consisting of a quasi-cubical cluster projectile of 40 atoms impacting on a 13500-atom cubic target. The analysis is carried out for six different supersonic initial velocities of the projectile, ranging from 6 km/s to 16 km/s. After the impact of the nano-projectile on the target, the system was studied from a structural and dynamical point of view. We present calculations of the pair correlation function, the common neighbour analysis and the density and temperature profiles at different times. According to our results, it is possible to distinguish two different regimes for this system. Nano-projectiles which impact at velocities lower than 8 km/s only produce a weak increase in the temperature and density and no important structural changes in the target. In contrast, impacts between 10 and 16 km/s produce significant increase of the temperature and density, leaving the target in an amorphous state.

1. Introduction

Hypervelocity impact of projectiles is a subject of great interest in basic and applied research, being relevant in several areas such as engineering and materials science, physics, aeronautics, mechanics, and among others [1]. For example, since the development of cluster beam technology in the 1980's, the quality of the beams and the number of applications continues to grow [2–4], as is the case of materials bombarded with cluster beams in order to clean or smooth their surface or to analyze their composition, as well as to consolidate clusters. In several cases, the effect of the cluster beams results from the combined action of single impacts, which occur separately and independently [5]. Therefore, it is important to understand the dynamics of each single impact. In the field of space applications, hypervelocity impacts are being studied to assess the damage they produce on ceramic tiles when nano and micrometeorites hit satellites, spacecraft and space stations. Because the experimental study at such high velocities (ranging from 3 km/s to 15 km/s approximately) is extremely difficult, computer simulation is an ideal tool to deal with it.

From the theoretical point of view, hypervelocity impacts are non-equilibrium phenomena which have been extensively treated at the macroscopic level, by using continuum hydrodynamic simulations [6], and only recently using molecular dynamics simulations, with the aim of bringing an understanding of these phenomena at the scale of inter-atomic interactions [7,8]. Besides the calculation of equilibrium properties and their associated fluctuations, molecular dynamics allows for a wider range of problems to be tackled: given that we have access to the atomic trajectories, we can study the transit to equilibrium as well as purely non-equilibrium phenomena (where we are interested not in the final state but in the process itself), for instance, shock-induced plasticity and fracture of materials. In this regard, Non-Equilibrium Molecular Dynamics (NEMD) has emerged recently as a branch dealing with, and promising to shed light on, the mechanism behind these (and other similar) irreversible processes [9].

In this work we describe the impact mechanisms consisting of a hypervelocity solid projectile hitting a target. Both the projectile and the target are made of copper, which is modeled by a realistic, many-body *embedded-atom* potential. The main goal is to describe the structural response of the target under six different impact velocities, ranging from 6.0 to 16 km/s. We provide a detailed description of the different processes, emphasizing the structural changes suffered by the target.

The paper is organized as follows: In Section 2 we explain the simulation procedure used, in Section 3 we present and discuss our results, and in Section 4 we draw the conclusions.

2. Simulation procedure

Several aspects should be taken into account to simulate this rather complex phenomena, like the choice of the interatomic

* Corresponding author.
E-mail addresses: nicorafa@gmail.com (N. Amigo), claudial.81@gmail.com (C. Loyola), sergdavis@gmail.com (S. Davis), gonzalo@fisica.ciencias.uchile.cl (G. Gutiérrez).

0927-0256/$ - see front matter © 2012 Elsevier B.V. All rights reserved.
http://dx.doi.org/10.1016/j.commatsci.2012.11.005

potential, the initial setup, as well as the proper descriptors in order to analyze the results.

2.1. Interaction potential

A major issue in atomistic simulation is the choice of the interatomic potential (or force field). In the case of copper, a number of interatomic potentials have been developed to study its behavior under different conditions of pressure and temperature. Most of them contain, in addition to a pairwise term, a many-body term under the generic names of *embedded-atom* potentials, *effective medium* potentials, *empirical tight-binding*, and so on [10–14]. The combination of two body and many body terms in the same interatomic potential is needed for metals in order to provide a good representation of the mechanical properties, including the Poisson ratio, which is impossible to obtain from a pair potential [15]. Among the several interatomic potential for copper, we adopt the Sutton–Chen potential [11], which is still simple and has been demonstrated to reproduce a number of experimental properties such as structure, density, elastic properties and melting temperature, allowing to perform realistic calculations on structural, thermophysical, mechanical and dynamical properties of the systems. The analytical expression of the Sutton–Chen interatomic potential energy, U, comprises a pair repulsion term plus a many-body cohesion term, and is given by

$$U = \sum_i U_i = \epsilon \sum_i \left(\sum_{j \neq i} \frac{1}{2} V(r_{ij}) - c\sqrt{\rho_i} \right), \tag{1}$$

where $V(r_{ij})$ is a pair potential defined by

$$V(r_{ij}) = \left(\frac{a}{r_{ij}} \right)^n, \tag{2}$$

accounting for the Pauli repulsion between the i and j atomic cores. The many body term, which captures the metallic bonding, is given by

$$\rho_i = \sum_{j \neq i} \left(\frac{a}{r_{ij}} \right)^m, \tag{3}$$

where ρ_i is the local density accounting for the cohesion associated with atom i. In these equations r_{ij} is the distance between atoms i and j, a is a length parameter scaling all spacings, c is a scale factor for the attractive terms, ϵ is an energy parameter, and m, n are integer parameters such that $m > n$. These parameters for pure Cu metal are shown in Table 1.

2.2. Setup of the system and simulation details

The impact of the projectile on the target, both composed of copper atoms, was simulated using *LPMD* software package [16], in the microcanonical (*NVE*) ensemble. Both objects consist of a *fcc* copper structure at room density $\rho = 8.97$ g/cm^3. The projectile was built as a 40 atoms cube with edge of 7.22 Å, and then thermalized at $T = 300$ K, rescaling the velocities to this value each 20 time steps, as is implemented in the LPMD package, resulting in a quasi-cubical cluster. The target is a 13,500 atoms cube with edge of 54.15 Å, and also was thermalized at $T = 300$ K, in the same way used for the projectile. Fig. 1 shows different views of the setup, with a projectile-target initial distance of 10.83 Å. In these and the following snapshots we use a color code from blue to red, where blue indicates the lowest temperature and red, the highest. An initial velocity v_0 was given to the projectile in such a way as the impact is in the < 1 0 0 > target direction. Six different values of v_0, namely 6, 8, 10, 12, 14 and 16 km/s were considered, which represent six independent simulations. The total simulation time was 13 ps, with a time step $\Delta t = 1$ fs.

Table 1
Parameters of the Sutton–Chen potential for Cu.

Metal	a (Å)	c	ϵ (eV)	m	n
Cu	3.61	39.755	0.0124	6	9

2.3. Structural analysis

A structural analysis was carried out at several different times during the impact. For that purpose, the pair correlation function and the common neighbors analysis were employed.

The pair correlation function, $g(r)$, allows us an atomic level description of the system, indicating whether it is in solid, liquid or amorphous state [17]. The partial pair correlation function $g_{\alpha,\beta}(r)$ is related to the probability $\langle n_{\alpha,\beta} \rangle$ of finding an atom of species β in a spherical shell between r and δr, which is centered in an atom of species α. This relation is given by

$$\langle n_{\alpha,\beta}(r, r + \delta r) \rangle = \rho_\beta 4\pi r^2 g_{\alpha,\beta}(r) \delta r, \tag{4}$$

where ρ_β is the number density of atoms of species β.

The common neighbor analysis (CNA) [18] is a tool used in atomistic simulations which allows us to determine the local ordering in a given structure. CNA gives more detailed information than the pair correlation function $g(r)$, as it considers not only the number of neighbors at a given distance but also their location with respect to other common neighboring atoms. In the CNA method, every pair of atoms is labeled according to four indices (i,j,k,l): the first index, i, is 1 for nearest neighbor pairs, 2 for next-nearest neighbors, and so on. The second index, j, corresponds to the number of *common neighbors* shared by the atoms in the pair. The third index, k, corresponds to the number of *bonds* that can be "drawn" between the j common neighbors (taking the bond length as the nearest neighbor distance). Finally, the fourth index, l, corresponds to the length of the longest chain that connects all the k bonds. In this study appear several set of indices, namely 1421, 1422, 1211, 1311. The group of indices 1421 and 1422 are of special importance, as they indicate the *fcc* and *hcp* crystal structures, respectively. For the groups 1211 and 1311 there is no well-known crystal structure associated to them, and in fact they resemble closely an amorphous structure.

3. Results

As an example of the six simulations performed, in Fig. 2 we show snapshots of the impact when the initial velocity of the projectile is $v_0 = 16$ km/s. The colors of the target indicate the temperature, as already mentioned. In this particular case, the projectile becomes totally destroyed, and its impact on the target generates high temperature and density wave front advancing in the < 1 0 0 > direction, which produces severe alterations in the atomic structure of the target. For the quantitative analysis of the impact process, the target was divided into two parts, which are displayed in Figs. 3 and 4.

The first one considered a study of the density and temperature profiles along the impact direction. In this case, the target was divided into 15 identical regions (bins), transverse to the impact direction, each one containing 900 atoms. The density and the temperature of each bin were evaluated for different times of the simulation, without taking into account the atoms of the projectile.

The second part of the analysis consisted in the structural study of the target. Fig. 4 shows how the target was divided into three zones. The first one is a cube of 405 atoms and an edge of ~18 Å, placed in the impact zone. The second one is a cubic shell with

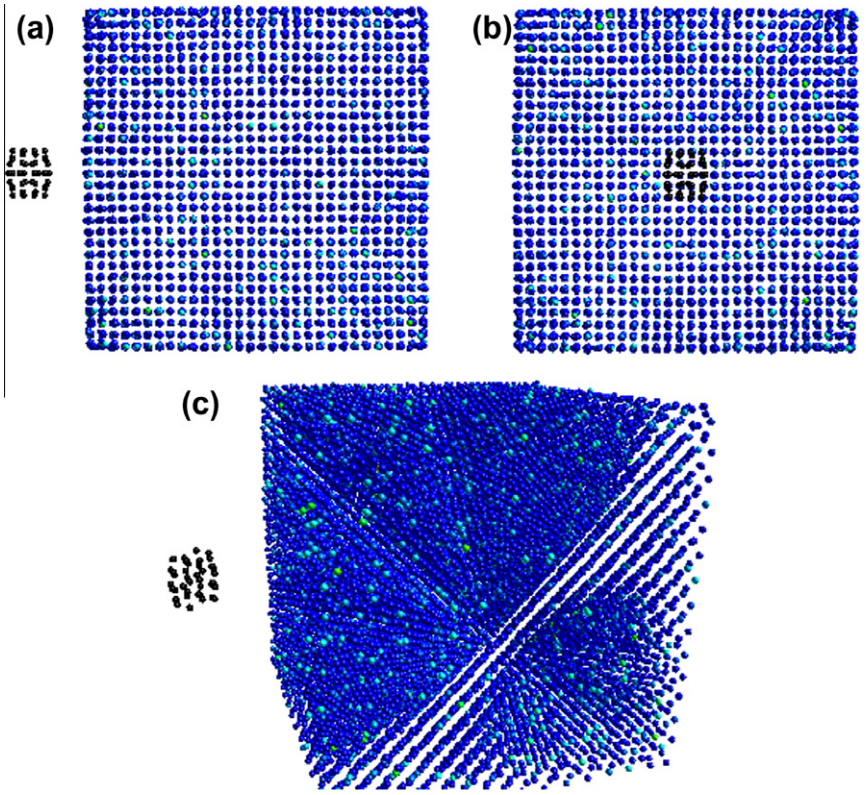

Fig. 1. Initial configuration of the projectile-target system. Both structures are thermalized at $T = 300$ K. The projectile is shown in black and the target, in a range from blue to red, where blue indicates the lowest temperature and red, the highest. (a) Side view of the projectile-target system. (b) Front view of the system. The projectile is pointing to the center of the target. (c) Three-dimensional, perspective view of the system.

an edge of ∼38 Å, width ∼15 Å, containing 4225 atoms and hollowed out in the impact direction. This shell surrounds zone 1 of the cube. Finally, the third zone is another cubic shell with an edge of 54.15 Å, width ∼13 Å, containing 10,163 atoms and also hollowed out in the impact zone. In Fig. 4b are shown zone 2 and 3 and their respective widths. Further, the last shell surrounds zone 2 and it also contains some atoms of the latter. Note that the sum of atoms of all the zones gives a total number higher than the total number of atoms in the system. Fig. 4c gives a front view of the shell corresponding to zone 3. In it, a big gray area can be observed, which surrounds zone 2. Furthermore a little dashed area, of width 3 Å, can be seen. It belongs to zone 2 but it also form part of zone 3. This is the area, already mentioned, which shares atoms with both zones. The white hole represents the rest of the zone 2. For studying the structure, the pair correlation function $g(r)$ and the common neighbor analysis CNA were evaluated during the simulation only in the zones 2 and 3. Zone 1 was not considered, as it does not contain enough atoms for reliable statistics, and because it contains the impact zone. The atoms of the projectile were not considered. The time origin, 0.00 ps, was taken as the projectile-target impact time.

3.1. Impact at 6 km/s and 8 km/s

A general overview of the projectile impact at the initial velocity of $v_0 = 6$ km/s can be observed in Fig. 5, at three different times, $t = 0.08$, 0.30 and 13.00 ps. From these snapshots can be inferred that at the beginning (Fig. 5a), due to the energy gained in the impact, a sudden increase of the temperature occurs, which is accompanied by a small increase in density which quickly disappears. Then, as shown in Fig. 5b, the perturbation propagates mainly across the $<1\,1\,0>$ direction. At the end, the impact energy is equally distributed among all the atoms of sample. A more precise picture can be deduced from Fig. 6a and b, where the density and temperature profiles are presented, respectively. Just as the projectile hits the target, an increase of temperature about 800 K is observed (Fig. 6a). Then, a rarefaction wave appears at $t = 0.10$ ps, causing a density decrease. After that, at $t = 0.60$ ps approximately, both fronts become quite weak. Nevertheless, the target is left with a temperature greater than the original 300 K. Note that the highest temperature is reached at times earlier than the instant in which the highest density is reached. That is because when the projectile impacts on the target, a large amount of energy is transferred, which causes a fast increment of temperature. Afterward, a compression wave is generated (followed by a rarefaction wave) which increases the density.

In Fig. 7 the common neighbor analysis and the pair correlation function for the zones 2 and 3 of the target can be seen, at different times. Fig. 7a shows the CNA of the zone 2, where the highest percentage corresponds to the indices 1421, fcc structure. Between $t = 0.00$ and 2.00 ps, fcc structure decreases approximately from 90% to 75% and a low percentage of amorphous structures (indices 1422 y 1311) appear, but then, around $t = 4.00$ ps, they decrease and the fcc structure percentage goes back to its normal value. Also, a low percentage (10%) of hcp crystal structure is always present. Fig. 7b displays the pair correlation function at the zone 2. It decreases at $t = 1.00$ ps (corresponding to the instant at which the fcc structure reaches the minimum value in Fig. 7a), but afterwards, at $t = 8.00$ ps, the distribution recovers its initial shape. In Fig. 7c and d the CNA and the pair correlation function corresponding to zone 3 is shown. A similar phenomena can be appreciated, but weaker and with a delay of 2.00 ps. This occurs due to the lower intensity of the compression wave in zone 3 and the longer time it takes in reaching it.

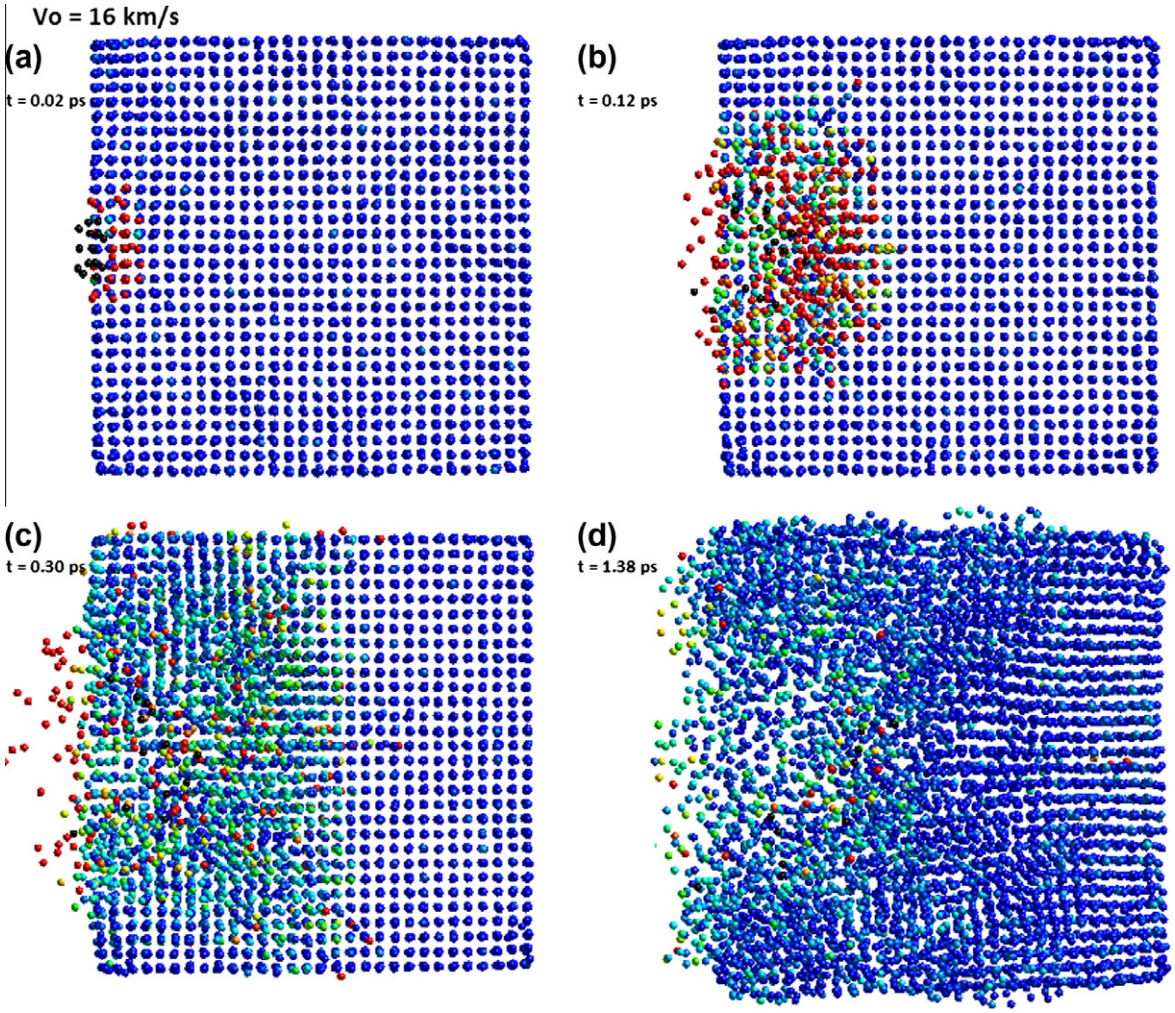

Fig. 2. Impact of the projectile, at $v_0 = 16$ km/s, on the target at different times. (a) At $t = 0.02$ ps the projectile impacts on the target generating an increment of the local temperature. (b) At $t = 0.12$ ps a temperature and density front is generated, which propagates through the target. (c) At $t = 0.30$ ps the projectile is completely disintegrated and the target is affected because of the temperature and density front. (d) At $t = 1.38$ ps the structural disorder of the target increases.

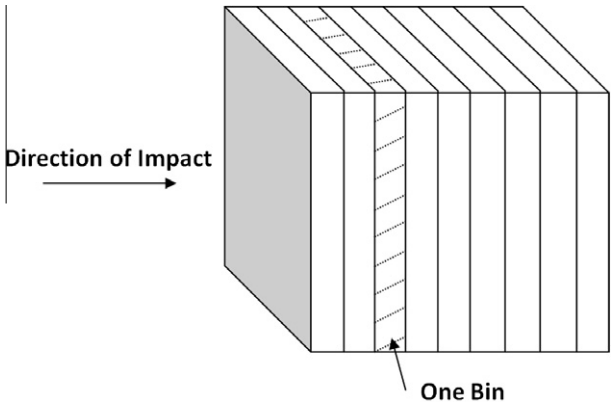

Fig. 3. The target is divided into 15 bins, transverse to the impact direction, for calculating the temperature and density profile in that direction. Each bin contains 900 atoms.

In the case of the impact at the initial velocity of $v_0 = 8$ km/s the situation is similar to the previous one, the main difference being that the temperature and density fronts are stronger. For example, the maximum density and temperature are about 9.4 g/cm^3 and 1800 K respectively. At the end, the target is left at a temperature between 400 and 700 K, and the fcc structure is about 60% in zone 2 and 80% in zone3.

3.2. Impact at 10 km/s and 12 km/s

Here we begin to observe a qualitatively different situation with respect to the previous ones. Fig. 8 shows a general aspect of the collision at three different times, $t = 0.12$, 0.30 and 13.00 ps, where is apparent that at the end the target suffers an important damage. Fig. 9 shows the density and temperature, with a maximum density $\rho \approx 9.5$ g/cm^3 and temperature $T \approx 2900$ K, Fig. 9a and b respectively. Note that the temperature of the target in the very late instants is higher than in the previous cases (when $v_0 = 6$ and 8 km/s).

The structural analysis shown in Fig. 10 reveals the salient feature of this process. The CNA in zones 2 and 3 (Fig. 10a and c respectively) shows a clear decrease in the fcc structure. Although its percentage increases in later times, it does not exceed 70%, rather low compared to the initial one, around 88%. Furthermore, around 10% of amorphous structures appear at $t = 1.00$ ps. The pair correlation function showed in Fig. 10b and d reveals a decrease of its peaks after the impact and in contrast to the previous cases, it basically remains in that state (with the exception of the peaks

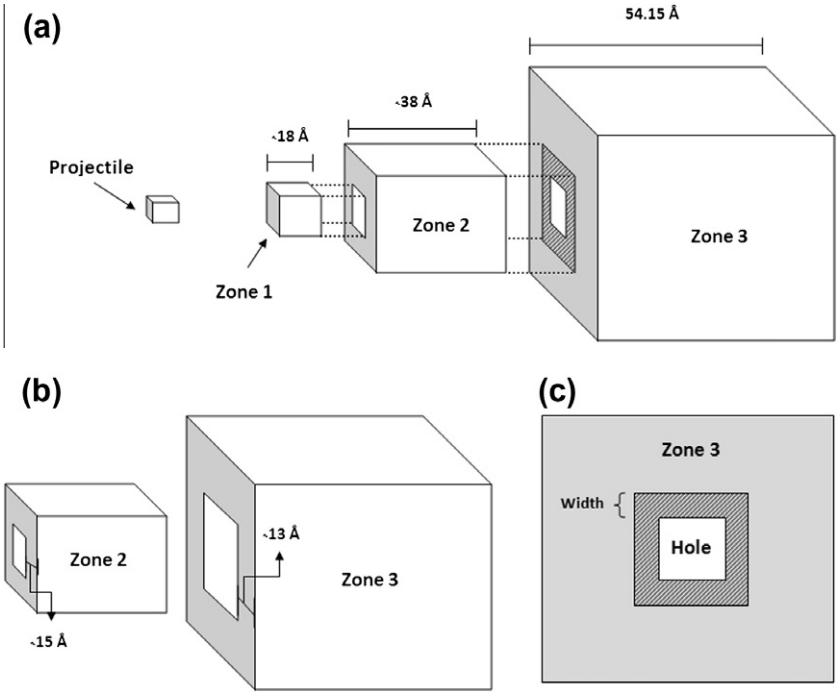

Fig. 4. (a) Projectile (left side) and target (right side), the latter divided into three zones for the structural analysis. Zones 1, 2 and 3 contain 405, 4225 and 10,163 atoms respectively. The dark gray dashed area represents the atoms being shared by zones 2 and 3. The length of the edges are included. (b) Zones 2 and 3 are shown with their respective widths. (c) Cubic shell corresponding to the zone 3. The dashed area belongs to the zone 2 and 3. It has a width of 3 Å. The white hole represents the rest of the zone 2.

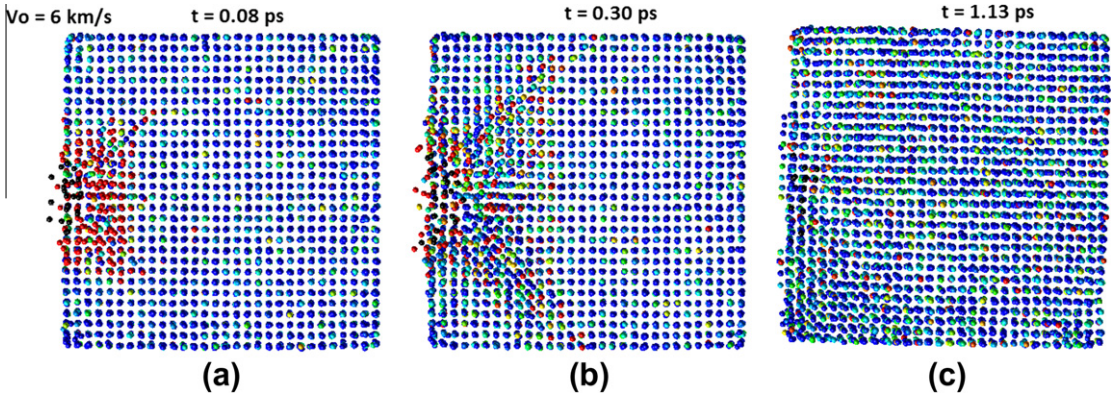

Fig. 5. Collision at $v_0 = 6$ km/s. (a) At $t = 0.08$ ps the projectile already disintegrated (b) At $t = 0.30$ ps the heat propagates through the target. (c) At the end, $t = 13$ ps, the target is still in a crystalline state.

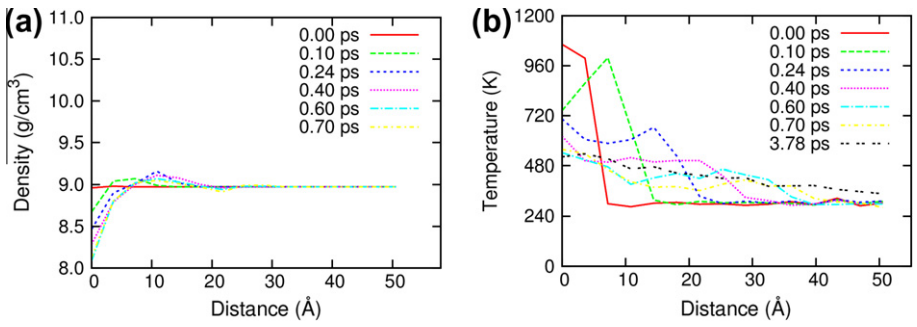

Fig. 6. Density and temperature profiles, $v_0 = 6$ km/s. (a) A density front is generated when the impact occurs, accompanied by a rarefaction wave. (b) The temperature at some bins reaches almost 1100 K. At $t = 0.60$ ps the temperature and density fronts go down but the initial bins of the target are left disordered. At $t = 3.78$ ps the target is left at higher temperature than the initial one.

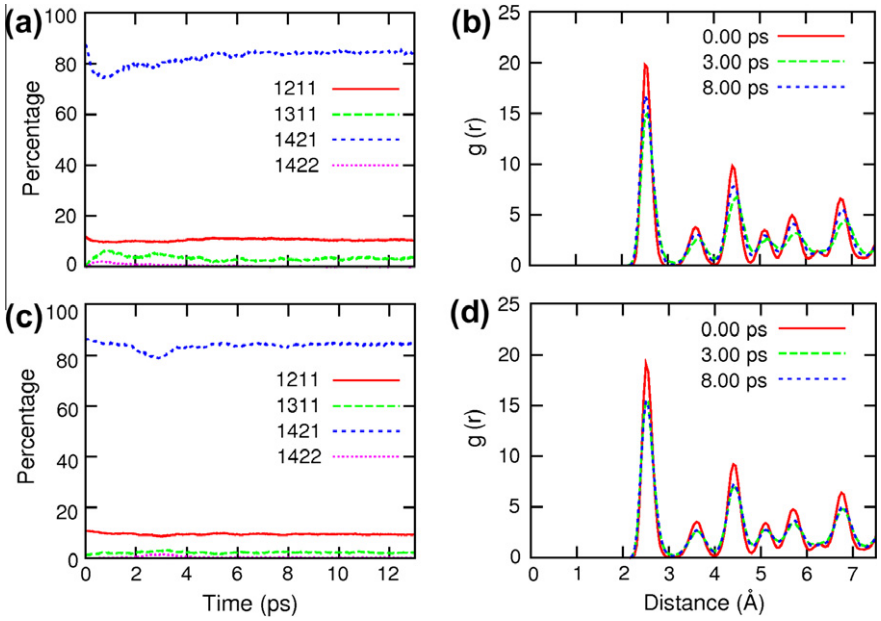

Fig. 7. CNA and pair correlation function, $v_0 = 6$ km/s. (a) The fcc structure percentage in zone 2 decreases a bit at $t = 1.00$ ps. The process is accompanied with the formation of an amorphous structure. (b) The pair correlation function corresponding to zone 2 decreases and then it increases softly. (c) and (d) CNA and $g(r)$ corresponding to zone 3. The phenomena already described is seen again but with a delay of 2.00 ps approximately and lesser magnitude.

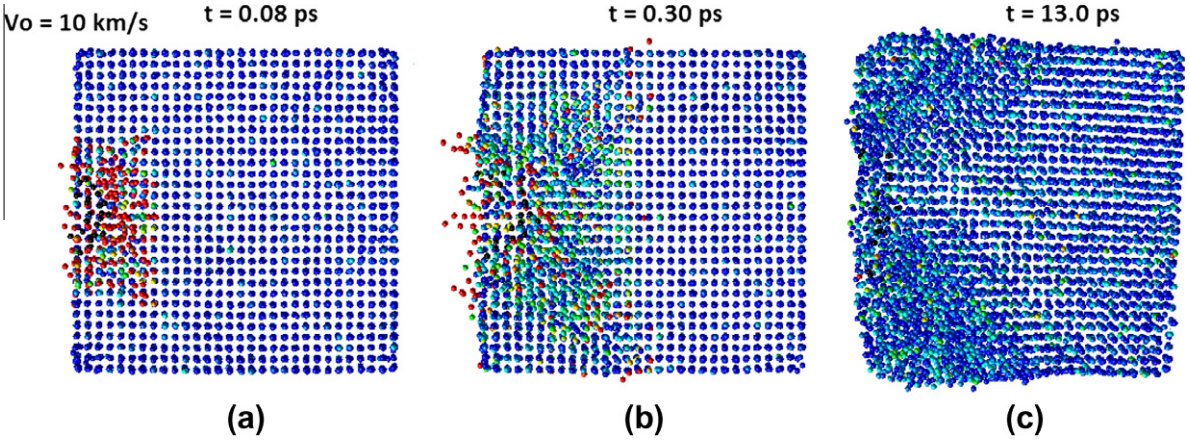

Fig. 8. Collision at $v_0 = 10$ km/s. (a) At $t = 0.08$ ps the projectile already disintegrated. (b) At $t = 0.30$ ps an increase of temperature and a density front propagate through the target. (c) At $t = 13.0$ ps part of the target has lost its crystalline structure.

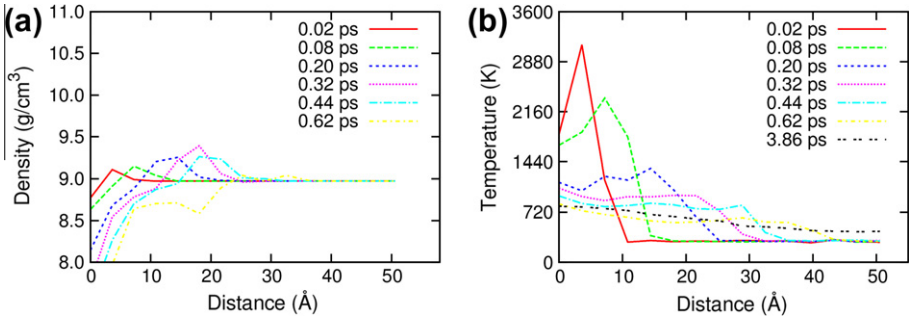

Fig. 9. Density and temperature profiles, $v_0 = 10$ km/s. (a) A density front and a rarefaction wave is generated. (b) A maximum temperature of approximately $T = 3000$ K is obtained. Important changes in temperature and density are present.

localized in 2.5, 4.4 and 6.75 Å). From these results it can be inferred that the target is left in a slightly amorphous state.

The situation at 12 km/s is similar to the $v_0 = 10$ km/s, but sharper. After the impact, the temperature of the target is about

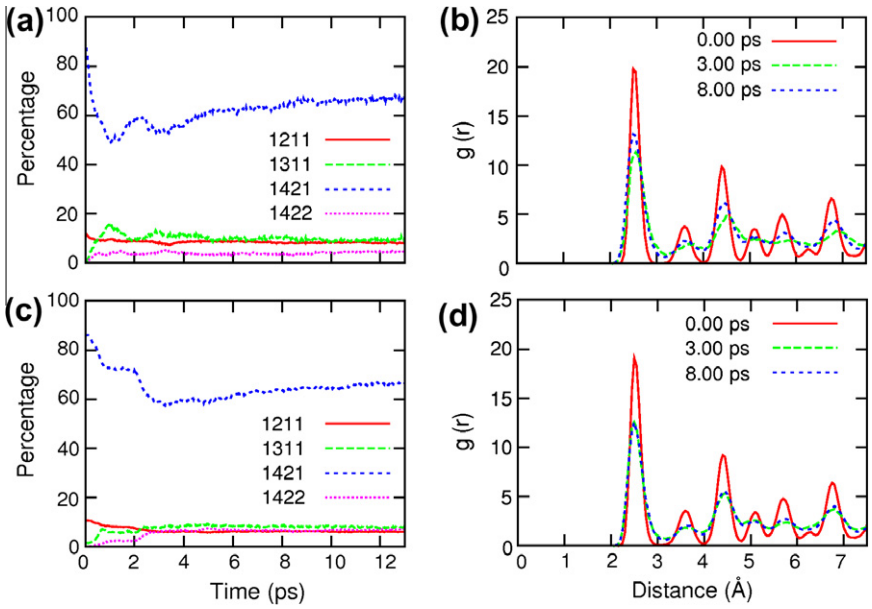

Fig. 10. CNA and pair correlation function, $v_0 = 10$ km/s. (a) and (c) A drastic decrease of the fcc structure percentage is observed in both zones. (b) and (d) The peaks of the pair correlation function decrease after the impact, except for the peaks at 2.5, 4.4 y 6.75 Å.

800–1000 K and there exists 40% of fcc structure in zone 2 and 50% in zone 3, increasing the amorphous structure up to 30%.

3.3. Impact at 14 km/s

The impact at $v_0 = 14$ km/s, left the target in an almost completely amorphous state, as can be seen in Fig. 11.

Fig. 12a shows the density profile, where a strong rarefaction wave can be distinguished. In Fig. 12b temperatures of almost 5500 K are observed. After $t = 0.44$ ps the target presents high temperatures and low densities in certain regions, reaching at the end about 900 K.

From Fig. 13a and b it can be inferred that zone 2 is in an almost completely disordered state, composed by several different structures, each of one with no more than 20%. This picture is reinforced by a flattened pair correlation function, characteristic of an amorphous state. In contrast, from Fig. 13c and d a different situation can be inferred for zone 3, where fcc structure has a value around 40% and pair correlation function still has some slight peaks at 2.5, 4.4 and 6.75 Å. Thus, it seems that the rarefaction wave was not enough to amorphize zone 3, in contrast to zone 2.

3.4. Impact at 16 km/s

At the impact velocity $v_0 = 16$ km/s, the target becomes completely amorphous, similar to the previous case. Fig. 14a and b shows strong density and temperature fronts, respectively. The observed rarefaction wave sharply decreases the density at the initial regions of the target. After $t = 0.76$ ps, a decrease of the density to very low values can be observed. Further, at $t = 0.82$ ps the temperature is 1000 K higher than the initial temperature.

Zone 2 is left in a completely amorphous state, as can be deduced from Fig. 15a and b. There is no predominant structure in the CNA and the pair correlation is rather flat, with small peaks at 2.7, 4.4 and 6.8 Å. In zone 3, the fcc structure still dominates but it is just 5–10% higher than the others, as can be seen in

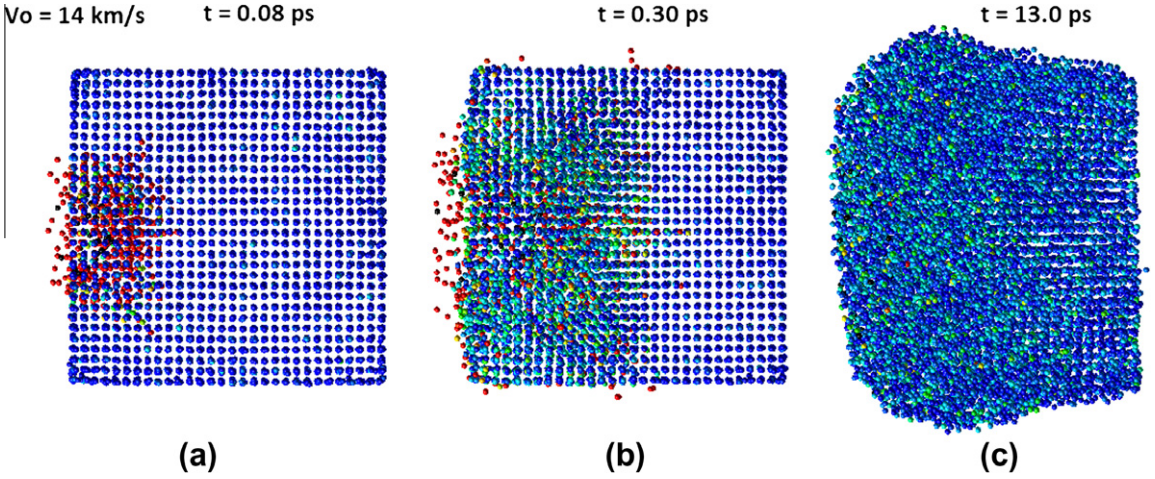

Fig. 11. Collision at $v_0 = 14$ km/s. (a) At $t = 0.08$ ps the projectile already disintegrated. (b) At $t = 0.30$ ps a strong temperature and density front can be observed. (c) At $t = 13.0$ ps most of the target has lost its crystalline state.

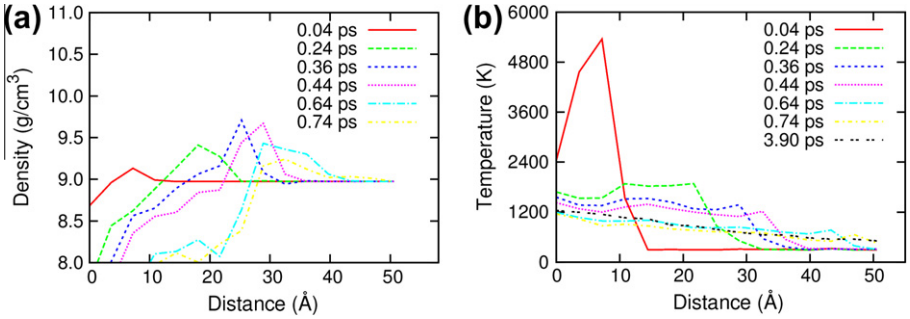

Fig. 12. Density and temperature profiles, v_0 = 14 km/s. (a) and (b) Strong density and temperature fronts are observed. Rarefaction wave can be clearly distinguished. After t = 0.30 ps the target suffers important damage because of the mentioned fronts. At the end, temperature is about 900 K higher than the initial temperature.

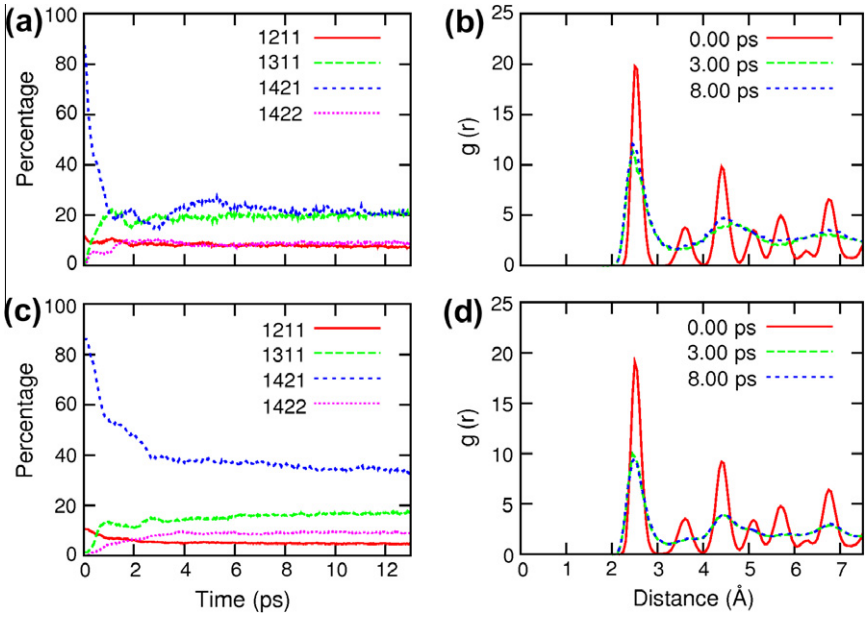

Fig. 13. CNA and pair correlation function, v_0 = 14 km/s. (a) Zone 2 has no predominant atomic structure. (b) $g(r)$ shows no definite peaks except for those at 2.5, 4.4 and 6.75 Å, indicative of an amorphous structure. (c) and (d) Zone 3 has a predominant atomic structure, namely, the fcc structure, but also has an important amount of amorphous structure. Pair correlation function has short and broad peaks at 2.5, 4.4 and 6.75 Å.

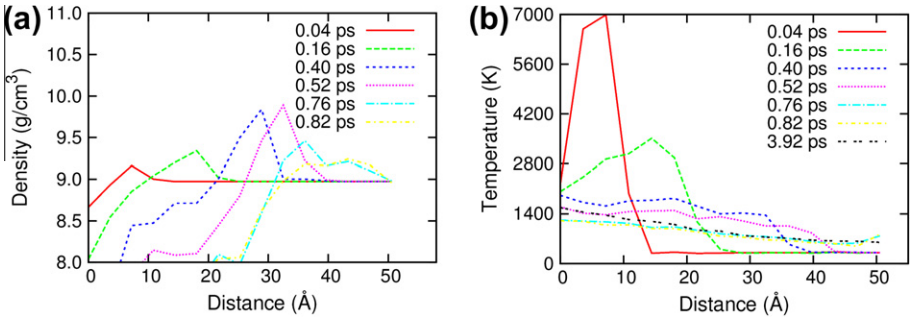

Fig. 14. Density and temperature profiles, v_0 = 16 km/s. (a) and (b) Strong density and temperature fronts are observed. The rarefaction wave is very strong and at t = 0.82 ps the temperature is almost 1000 K higher than the initial one. The target remains at a temperature quite higher than the initial one after the impact.

Fig. 15c. Fig. 15d shows that at zone 3 the pair correlation function is also rather flat, with few small and smooth peaks. Thus, the target is completely in an amorphous state.

3.5. Transition from crystalline to amorphous state

In order to have a general overview and a better understanding of the hypervelocity impact and its consequences, we present here an analysis of the results in terms of the different impact velocities. The previous results show that after the impact, in addition to the temperature-density wave front, a rarefaction wave is transmitted through the target. The higher the impact velocity, the stronger is the rarefaction wave. This is easily inferred from the temperature and density profiles shown in Fig. 16a and b, at t = 2.00 ps, for the six different initial velocities. Pair correlation function for zone 2 and 3 is shown for the same

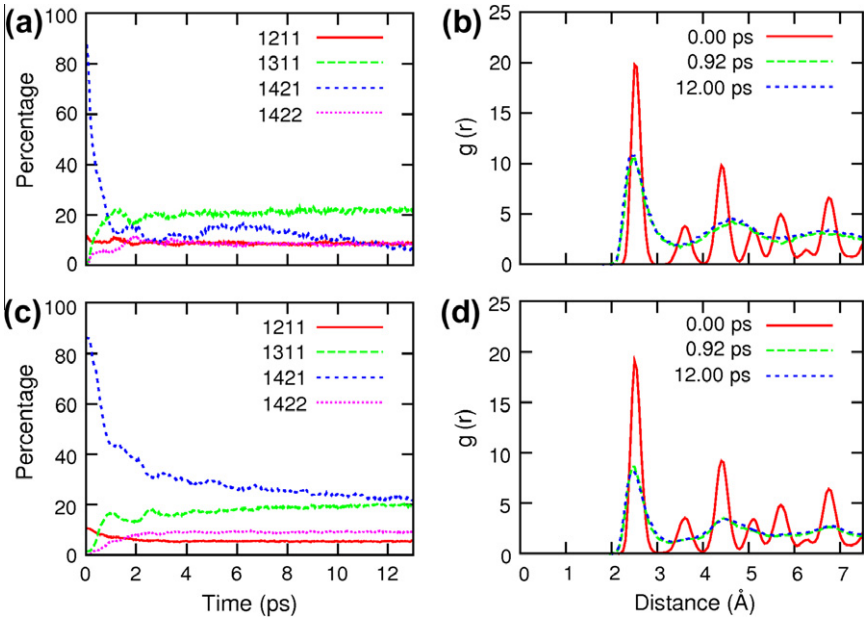

Fig. 15. CNA and pair correlation function, $v_0 = 16$ km/s. (a) The CAN shows no predominant crystal structure in zone 2. (b) There are distinguishable peaks only at 2.7, 4.4 and 6.8 Å. (c) In the zone 3, the CNA shows that fcc structure percentage is just a bit higher than the others. (d) Pair correlation function is similar to the one of zone 2. The target is left in a completely amorphous state.

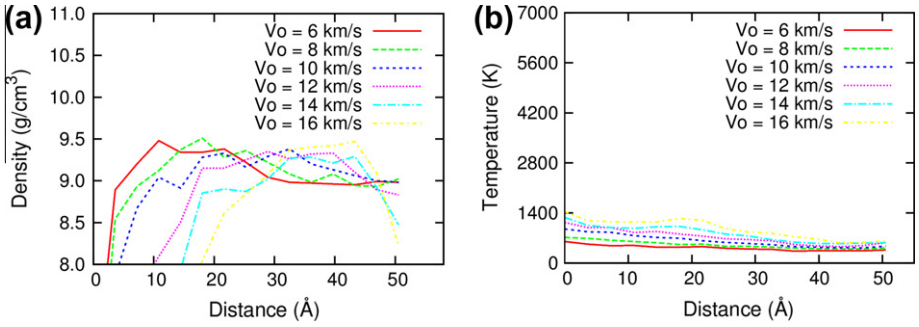

Fig. 16. (a) Density and (b) temperature profiles at $t = 2.00$ ps for all impact velocities. The density presents significant variations across the sample. The temperature is higher for faster impacts.

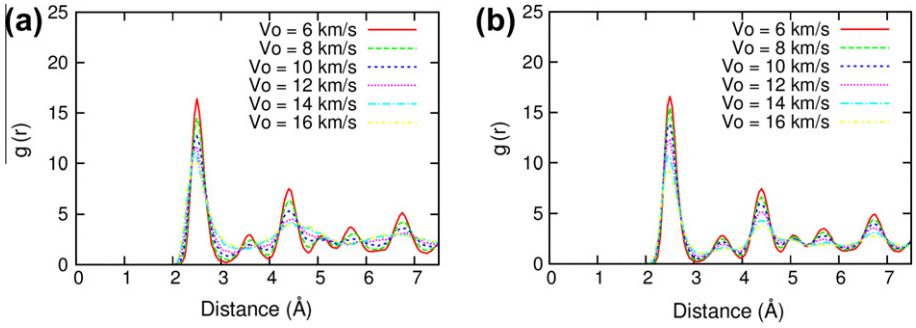

Fig. 17. Pair correlation function for (a) zone 2 and (b) zone 3, at $t = 2.00$ ps for all the impact velocities. The curve becomes flatter for $v_0 = 14$ and $v_0 = 16$ km/s, suggesting an amorphous state.

time and impact velocities in Fig. 17a and b, respectively. In zone 2, the peaks of $g(r)$ decrease when impact velocity increases, as can be seen clearly for $v_0 = 6$ and $v_0 = 16$ km/s. For $v_0 = 14$ and $v_0 = 16$ km/s the curves look like the case of an amorphous state. Similar situation is found in zone 3, but sharper than zone 2. Fig. 18a and b shows the changes of fcc structures present in zone 2 and 3 as a function of time, respectively. The decrease of the fraction of fcc structure as measured by CNA at high impact velocity, $v_0 = 14$ and $v_0 = 16$ km/s, is consistent to the more disordered state happened at such velocities.

Finally, let us estimate the required velocity of the projectile to melt the target. The total energy required to do so, that is to

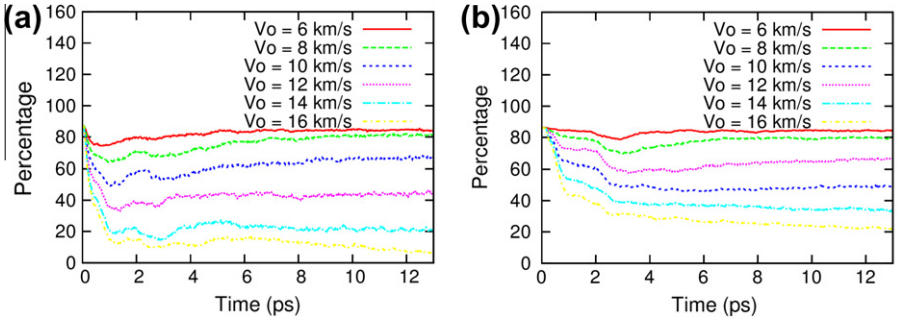

Fig. 18. Percentage of fcc structure in (a) zone 2 and (b) zone 3 for all the impact velocities along the simulation process.

increase the temperature from its initial value $T_0 = 300$ K to the melting temperature $T_m = 1358$ K plus the latent heat, is given by

$$E = \int_{T_0}^{T_f} Mc_p dT + ML, \tag{5}$$

where c_p is the specific heat capacity at constant pressure, L is the specific latent heat [19], and $M = 1.42 \times 10^{-21}$ kg is the mass of the target, which consists of 13,500 atoms. Considering the kinetic energy of the projectile the only source for this energy, that is $E = \frac{1}{2}mv^2$, with $m = 4.22 \times 10^{-24}$ kg the mass of the 40 atoms of the projectile, we obtain the velocity v needed for melting:

$$v = \sqrt{\frac{2}{m}\left(\int_{T_0}^{T_f} Mc_p dT + ML\right)} = 19.1 \text{ km/s}. \tag{6}$$

4. Conclusions

From the results obtained it is possible to distinguish two different final states, depending on the initial velocity of the projectile. At initial velocitie, $v_0 = 6$ and 8 km/s, a compression and a rarefaction wave develops across the sample, producing local disorder, but later on the target recovers a great part of its original crystalline structure, composed mainly by fcc structures (more than 80%).

On the other hand, at higher impact velocities ($v_0 = 10$–16 km/s), a different final state is verified. In this case, the projectile causes a large amount of disorder, even momentarily melting part of the sample, becoming amorphous at the end of the process. In particular, it can be seen that the initial fcc structure decreases to around 10%, being the amorphous structure the predominant one. Moreover, a simple thermodynamic calculation allows us to estimate that sending the projectile faster that 19 km/s should melt the sample.

All in all, we presented an hypervelocity impact simulation which, in spite of its size, allows us to extract quantitative and qualitative information that sheds some light on this complex phenomenon.

Acknowledgments

NA thanks Conicyt fellowship. CL acknowledges Conicyt Postdoctoral fellowship. SD acknowledges partial support from Fondecyt 3110017 and GG to ENL 10/06 VRID–Universidad de Chile and Fondecyt 1120603.

References

[1] P.S. Branicio, R.K. Kalia, A. Nakano, P. Vashishta, F. Shimojo, J.P. Rino, Journal of the Mechanics and Physics of Solids 56 (2008) 1955–1988.
[2] D. Jacquet, Y.L. Beyec, Nuclear Instruments and Methods in Physics Research B 193 (2002) 227.
[3] A. Kirkpatrick, Nuclear Instruments and Methods in Physics Research B 206 (2003) 830.
[4] V.N. Popok, E.E.B. Campbell, Reviews on Advanced Materials Science 11 (2006) 19.
[5] H. Hsieh, R.S. Averback, H. Sellers, C.P. Flynn, Physical Review B 45 (1992) 4417.
[6] K.S. Holian, B.L. Holian, International Journal of Impact Engineering 8 (1989) 115–132.
[7] J. Samela, K. Nordlund, Physical Review B 76 (2007) 125434.
[8] C. Zhang, R.K. Kalia, A. Nakano, P. Vashishta, Applied Physics Letters 91 (2007) 071906.
[9] M. Allen, D. Tildesley, Computer Simulation of Liquids, Clarendon Press, Oxford, 1987.
[10] M.S. Daw, M.I. Baskes, Physical Review B 29 (1984) 6443–6453.
[11] A.P. Sutton, J. Chen, Philosophical Magazine Letters 61 (1990) 139–164.
[12] G.J. Ackland, D.J. Bacon, A.F. Calder, T. Harry, Philosophycal Magazine A 75 (1997) 713–732.
[13] P. Heino, H. Hakkinen, K. Kaski, Europhysics Letters 41 (1998) 273–278.
[14] Y. Mishin, D. Farkas, M.J. Mehl, D.A. Papaconstantopoulos, Physical Review B 59 (1999) 3393–3407.
[15] V. Vitek, MRS Bulletin 21 (1996) 20–23.
[16] S. Davis, C. Loyola, F. González, J. Peralta, Computer Physics Communications 181 (2010) 2126–2139.
[17] G. Gutiérrez, E. Menéndez-Proupin, C. Loyola, J. Peralta, S. Davis, Journal of Material Science 45 (2010) 5124–5134, http://dx.doi.org/10.1007/s10853-010-4579-0.
[18] C. Loyola, S. Davis, J. Peralta, G. Gutiérrez, Computational Materials Science 49 (2010) 582–587, http://dx.doi.org/10.1016/j.commatsci.2010.05.052.
[19] R. Perry, D. Green, Perry's Chemical Engineers' Handbook, Mc Graw Hill, 1999.